

Brief Report

Spatiotemporal Evolution and Drivers of the Four Ionospheric Storms over the American Sector during the August 2018 Geomagnetic Storm

Changzhi Zhai * , Yutian Chen, Xiaoyun Cheng and Xunzhe Yin

School of Earth Sciences and Engineering, Hohai University, Nanjing 211100, China

* Correspondence: czzhai@hhu.edu.cn

Abstract: The spatiotemporal variations and mechanisms of the ionospheric storms over the American sector during the August 2018 geomagnetic storm are investigated. One positive and one negative ionospheric storm occurred in North America and two positive storms were observed in South America. The ionosphere showed prominent hemispheric asymmetries during the four storms. The maximum VTEC (vertical total electron content) variation was more than 15 TECU during the positive storms and about -10 during the negative storm. The GUVI (Global Ultraviolet Imager) oxygen (O) to nitrogen (N₂) column density ratio ($\Sigma O/N_2$) and SuperDARN (Super Dual Auroral Radar Network) polar cap potential results showed that the electric field variations played a decisive role in generating the North American negative storm while the thermospheric composition changes were responsible for the North American positive storm and the two South America positive storms.

Keywords: ionospheric storm; neutral wind; neutral composition; electric field; polar cap potential



Citation: Zhai, C.; Chen, Y.; Cheng, X.; Yin, X. Spatiotemporal Evolution and Drivers of the Four Ionospheric Storms over the American Sector during the August 2018 Geomagnetic Storm. *Atmosphere* **2023**, *14*, 335. <https://doi.org/10.3390/atmos14020335>

Academic Editors: Victor Ivanovich Zakharov, Xuguang Cai, Tingting Yu and Ercha Aa

Received: 19 December 2022

Revised: 29 January 2023

Accepted: 6 February 2023

Published: 7 February 2023



Copyright: © 2023 by the authors. Licensee MDPI, Basel, Switzerland. This article is an open access article distributed under the terms and conditions of the Creative Commons Attribution (CC BY) license (<https://creativecommons.org/licenses/by/4.0/>).

1. Introduction

Due to the impacts on radio communications, satellite navigation, and space craft, the studies of ionospheric disturbances during geomagnetic storms have been carried out for several decades [1–6]. When the high-speed interplanetary plasma passes the Earth with southward Bz component, a large amount of energy from the magnetosphere and solar wind is conveyed into the Earth's ionosphere and thermosphere [7–11]. Ionospheric electron density variations during the geomagnetic storms—compared to quiet time—can increase and decrease, which are referred to as “positive” [12–18] and “negative” [19–22] ionospheric storms, respectively.

The ionosphere is affected by a number of externally and internally driven dynamic and electrodynamic processes. During geomagnetic storms, electric fields are strongly significantly enhanced by a strong southward interplanetary magnetic field (IMF) point from dawn to dusk across the polar cap. The dawn-to-dusk electric fields can penetrate to middle and low latitudes. On the dayside, the eastward prompt penetration electric fields (PPEFs) cause plasma vertical drift along the geomagnetic field lines, and the lifted plasma accumulates due to the lower recombination rate at high altitudes and generates VTEC enhancements [12,23]. In addition, PPEFs can penetrate into low latitude and enhance the fountain effect, and the Equatorial ionization anomaly (EIA) crest would shift to higher latitudes and cause plasma density enhancements [16,17,24]. The equatorward neutral wind induced by Joule and particle heating at the auroral area can also push ionospheric plasma upward along magnetic lines and cause positive variations [14,25].

In addition to the electrodynamic coupling of the solar wind/magnetosphere/ionosphere, the chemical processes between thermosphere and ionosphere can also disturb the plasma density [26]. When there is a geomagnetic storm, the bottom thermosphere at high latitudes expands due to Joule and participate heating. The upwelling transports heavier species from the lower thermosphere to higher altitudes and increases the relative abundance of heavier

species. The increase and decrease in molecular nitrogen (N_2) cause negative and positive ionospheric variations. In addition, the equatorward neutral wind surge can drive a westward wind component due to the Coriolis force, generating disturbance dynamo electric fields (DDEFs) [20,27,28] in the mid- and low-latitude ionosphere, which is opposite to that of the ambient zonal fields at the equator, which results in negative ionospheric effects.

A weak coronal mass ejection (CME) arrived at the Earth on 25 August 2018 and unexpectedly caused a major geomagnetic storm. Using multi-instrument approach from the solar surface to the Earth, Akala, et al. [29] analyzed the solar origins and suggested that the G3 geomagnetic storm was generated by an aggregation of weak coronal mass ejection (CME) transients and corotating interaction regions/high speed streams (CIR/HSSs). During the main and the recovery phases of the storm, prominent hemispheric asymmetries in the thermosphere and ionosphere were observed by GNSS VTEC, Swarm, and Global Ultraviolet Imager (GUVI) [30]. Bolaji et al. [31] compared different longitudinal ionospheric response to the geomagnetic storm and found that the fountain effect was restrained and enhanced during the main phase in the American and Asian/Australian sector, respectively. By using observations from multi-instruments, including GNSS, ionosondes, and satellites, Blagoveshchensky and Sergeeva [32] investigated the ionospheric response to this storm over the European sector. The results showed that the F2 layer was under a positive disturbance at mid and low latitudes during the main phase, while the recovery phase was dominated by a negative response. Mansilla and Zossi [33] analyzed the variations of foF2, hmF2, and TEC during the storm and suggested that foF2 showed decreases at equatorial and low latitudes and small increases at mid-latitudes. Using various parameters including TEC, geomagnetic field, and O/N_2 , [34] investigated ionospheric and magnetic signatures at low latitudes and midlatitudes during this storm. The results showed that the storm-induced thermospheric wind mainly affected dayside and duskside sectors, and the partial ring current (PRC) played an important role in ionospheric currents.

Although the origin of this storm and ionospheric response over different sectors have been investigated in previous studies, the evolution processes of different storms driven by different mechanisms over similar magnetic longitude are still unrevealed. In this study, a detailed spatiotemporal investigation and comparison of three positive and one negative ionospheric storms over the American sector are presented. Based on VTEC observations from the Massachusetts Institute of Technology (MIT) Haystack Observatory, the evolution and percentage variation of four storms are analyzed. Observations from GUVI and SuperDARN are also used to investigate the drivers of these four ionospheric storms.

2. Data and Methodology

2.1. Geomagnetic Environment Indices

Geomagnetic indices were downloaded from Coordinated Data Analysis Web (https://cdaweb.gsfc.nasa.gov/cdaweb/sp_phys/) (accessed on 22 August 2022). IMF Bz and By components are in geocentric solar magnetospheric (GSM) coordinates. The time resolution of IMF By, Bz, Auroral electrojet (AE), and Dst indices is 5 min. The intervals of Kp and F10.7 indices are 3 h and 1 day, respectively.

2.2. GNSS VTEC

The global GNSS VTEC data obtained from Massachusetts Institute of Technology Haystack Observatory Madrigal is used in this study. The spatial resolution is $1^\circ \times 1^\circ$ (latitude by longitude) and the temporal resolution is 5 min. The VTEC were generated by using GNSS data from more than 8000 receivers around the world and the detailed GNSS data processing algorithms were described in [35,36].

2.3. Thermospheric $\Sigma O/N_2$ Composition

The $\Sigma O/N_2$ composition observation was measured by the Global Ultraviolet Imager (GUVI) on board the Thermosphere, Ionosphere, Mesosphere Energetics and Dynamics (TIMED) satellite. The GUVI instrument measures a narrow swath of far ultraviolet airglow

from the upper atmosphere during the dayside spacecraft passages. The altitude of TIMED orbit is 625 km and the inclination is 74° [37].

2.4. Polar Cap Potential Map

To analyze the contributions from electric field to the ionospheric response, the polar cap potential map from Super Dual Auroral Radar Network (SuperDARN) is used in this study. The network consists of more than 30 low-power high-frequency (HF) radars over mid-latitudes and polar regions. The polar cap potential map is derived from the line of sight plasma velocity measurements with a spherical harmonic model over high latitudes [38].

3. Results

3.1. Event Overview

Figure 1 shows the geomagnetic conditions from 23 to 27 August in 2018. The vertical black line denotes the time of the CME arrival at 02:45 UT on 25 August [31]. In Figure 1a, IMF B_y increased gradually from 15:30 UT on 25 and reached 18.2 nT at ~09:00 UT on 26 August. B_z turned southward at ~15:20 UT on 25 August and decreased to -16 nT at 05:00 UT on 26 August. There were several fluctuations in B_z from ~10:00 UT to ~21:00 UT. During the time period when B_z turned from negative to fluctuations, the AE index increased from ~100 nT to ~2500 nT and also oscillated after the peak (Figure 1b). K_p increased from 1.7 at 15:00 UT on 25 August to 7.3 at 07:00 UT on 26 August and reduced to 1.3 at 01:00 UT on 27 August. As shown in Figure 1c, the Dst index started to gradually descend from ~17:30 UT on 25 August and reached the minimum of -207 nT at 05:00 UT on 26 August. The F10.7 index was between 70 and 75 during 25–27 August.

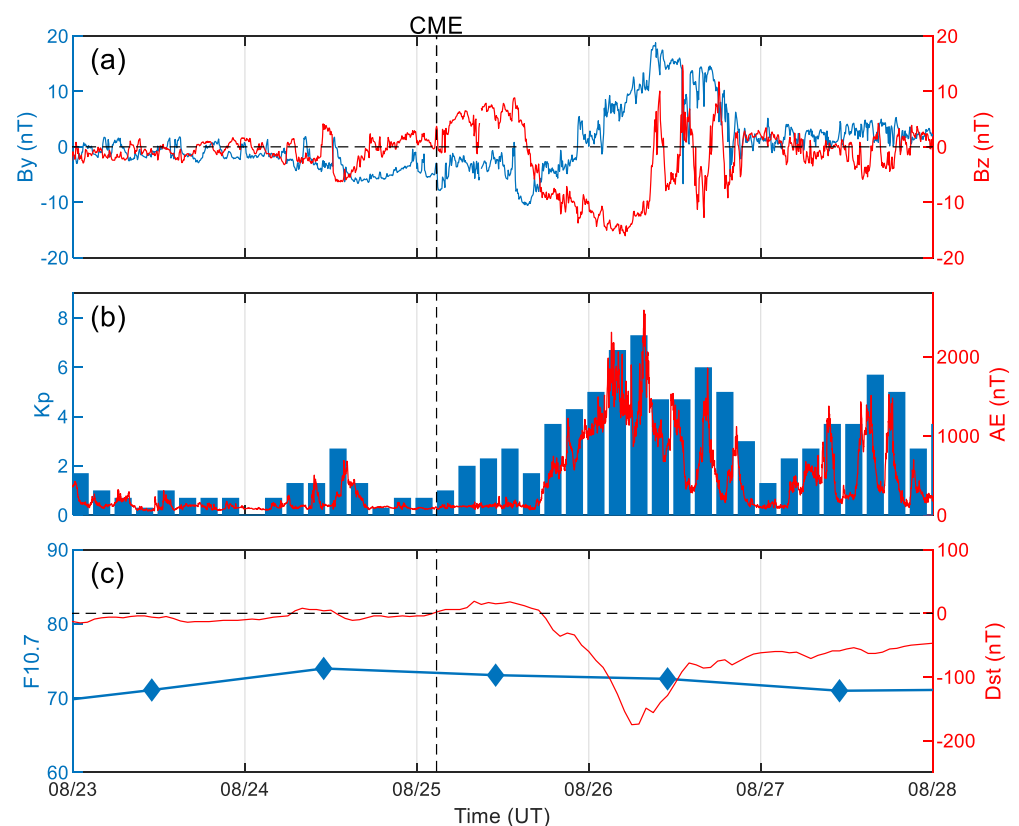


Figure 1. Geomagnetic conditions from 23 to 28 August in 2018. (a) IMF components of B_z and B_y in geocentric solar magnetospheric (GSM) coordinates. (b) the Auroral electrojet (AE) and K_p indices. (c) The F10.7 and Dst indices. The vertical black line denotes the arrival time of CME. The horizontal dashed line denotes zero value.

During the geomagnetic storm from 25 to 27 August, four ionospheric storms were observed by GNSS VTEC over the American sector. Figure 2 presents the VTEC difference distribution over the American sector between storm days (25–27 August) and the quiet day (23 August). At 22:00 UT on 25 August, a positive ionospheric storm occurred over the North American sector from $\sim 20^\circ$ N to 55° N, while no obvious VTEC variation was observed in South America. In Figure 2b, a positive storm was observed at 14:00 UT on 26 August over South America. At 02:00 UT on 27 August, a negative storm dominated North America while there was small positive ionospheric disturbance in South America. The fourth storm appeared around 16:00 UT on 27 August over South America. The ionospheric response in the American sector showed significant hemispheric asymmetries during the geomagnetic storm.

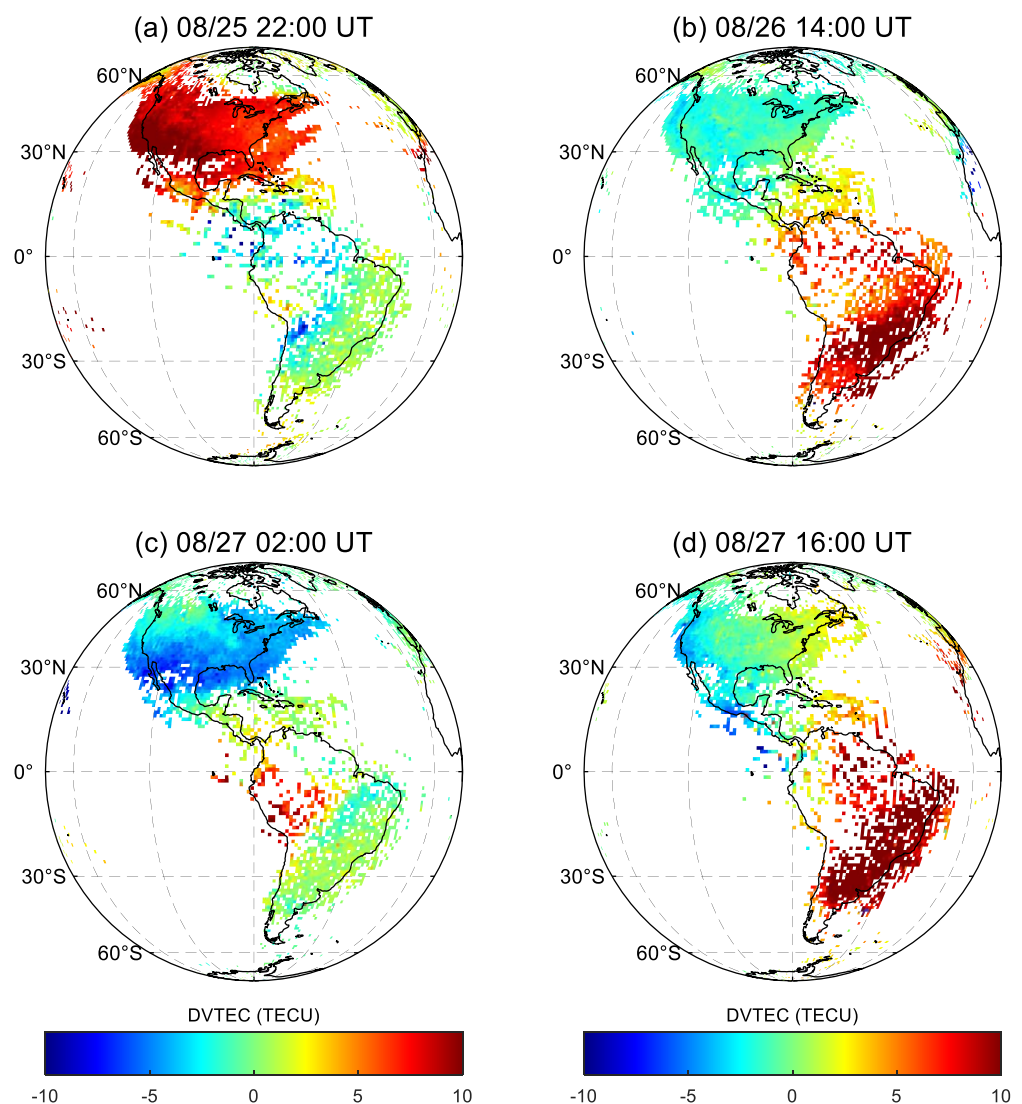


Figure 2. VTEC difference distribution over American sector between storm days (25–27 August) and quiet day (23 August).

The information for the four ionospheric storms is summarized in Table 1. For the convenience of expression, the four storms are named as storm-1, storm-2, storm-3, and storm-4.

Table 1. List of four ionospheric storms.

Region	Time	Variation	Name
North America	16:00 25 August–06:00 26 August	Positive	storm-1
South America	09:00 26 August–18:00 26 August	Positive	storm-2
North America	23:30 26 August–04:30 27 August	Negative	storm-3
South America	11:00 27 August–21:00 27 August	Positive	storm-4

3.2. Storm-1

Figure 3 gives the spatiotemporal evolutions of the VTEC difference during storm-1. The VTEC enhancement appeared at 16:00 UT on 25 August in the north of the North American sector with a magnitude about 4 TECU. From 18:00 to 22:00 UT, the enhancement region expanded from ~50° N to low latitude and the magnitude increased to ~15 TECU. At 02:00 UT on 26 August, the coverage of the positive storm decreased, and storm enhanced density (SED) and mid-latitude trough (MIT) structures were observed around 45° N. From 04:00 to 06:00 UT, the VTEC enhancement further decreased.

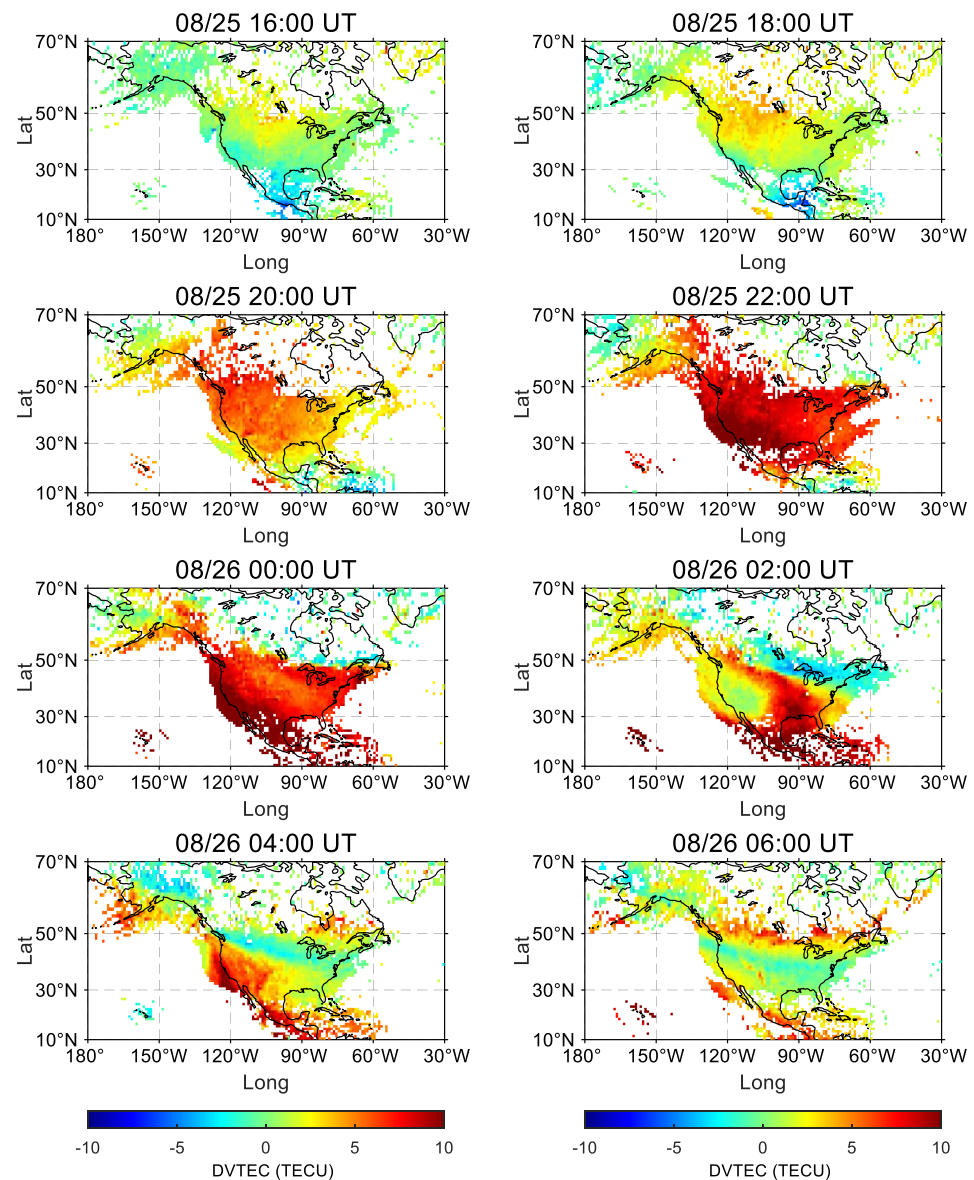


Figure 3. Spatiotemporal evolutions of the North American positive ionospheric storm.

To investigate the latitudinal and temporal variations of storm-1, the latitude/time variation of VTEC difference and relative VTEC difference at 110° W from 15° N to 60° N are given in Figure 4. As we can see in Figure 4a, the VTEC enhancement started from 60° N and expanded to lower latitudes gradually. The magnitude maximum of VTEC enhancement was ~ 15 TECU, which appeared from 22:00 UT on 25 to 02:00 UT on 26 August below 30° N. Figure 4b depicts the relative VTEC difference during the positive storm. Different from the magnitude distribution of VTEC difference, the maximal percentage difference was between 30 and 55° N from 20:00 UT on 25 to 01:00 UT on 26 August, which exceeded 200%.

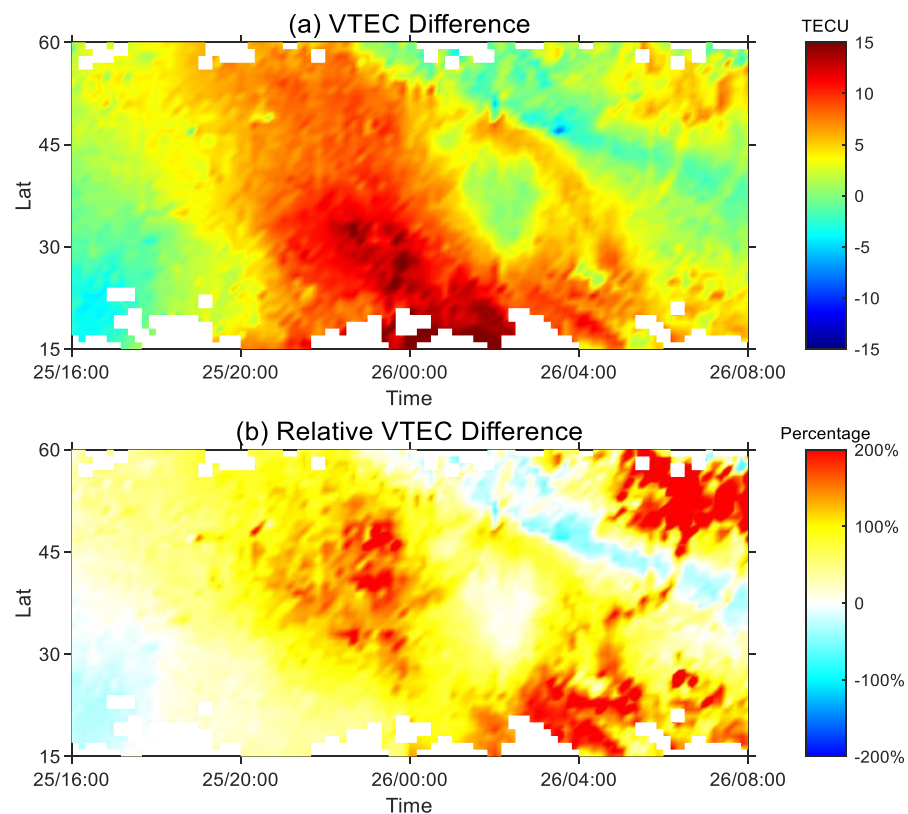


Figure 4. Latitude/time variation of (a) VTEC difference and (b) relative VTEC difference of the Storm-1 from 15° N to 60° N at 110° W.

3.3. Storm-2

The spatiotemporal evolutions of storm-2 are given in Figure 5. At 09:00 UT on 26 August, no ionospheric disturbance was observed over the South American sector. The VTEC enhancement first appeared in the northeast of South America. The VTEC enhancement extended to the whole South American sector from 10:00 UT to 14:00 UT and the magnitude increased to more than 15 TECU. At 16:00 UT, the enhancement decreased at low latitudes and there was no significant VTEC enhancement when the time came to 18:00 UT.

Figure 6 shows the latitude-time variation of VTEC difference and relative VTEC difference of storm-2 at 50° W. The VTEC enhancement appeared at $\sim 10^\circ$ N and $\sim 45^\circ$ S at 11:00 UT on 26 August and expanded to 20° S. As shown in Figure 6a, the latitudinal propagation direction of the positive storm was from low and high latitudes to middle latitudes. There were two salient VTEC enhancements which appeared at $\sim 13:00$ UT and 15–17:00 UT with the maximal magnitude of more than 15 TECU. In Figure 6b, the relative VTEC difference below 15° S was about 100%. The percentage of VTEC difference exceeded 200% from 11:00 to 14:00 UT between 20 and 45° S.

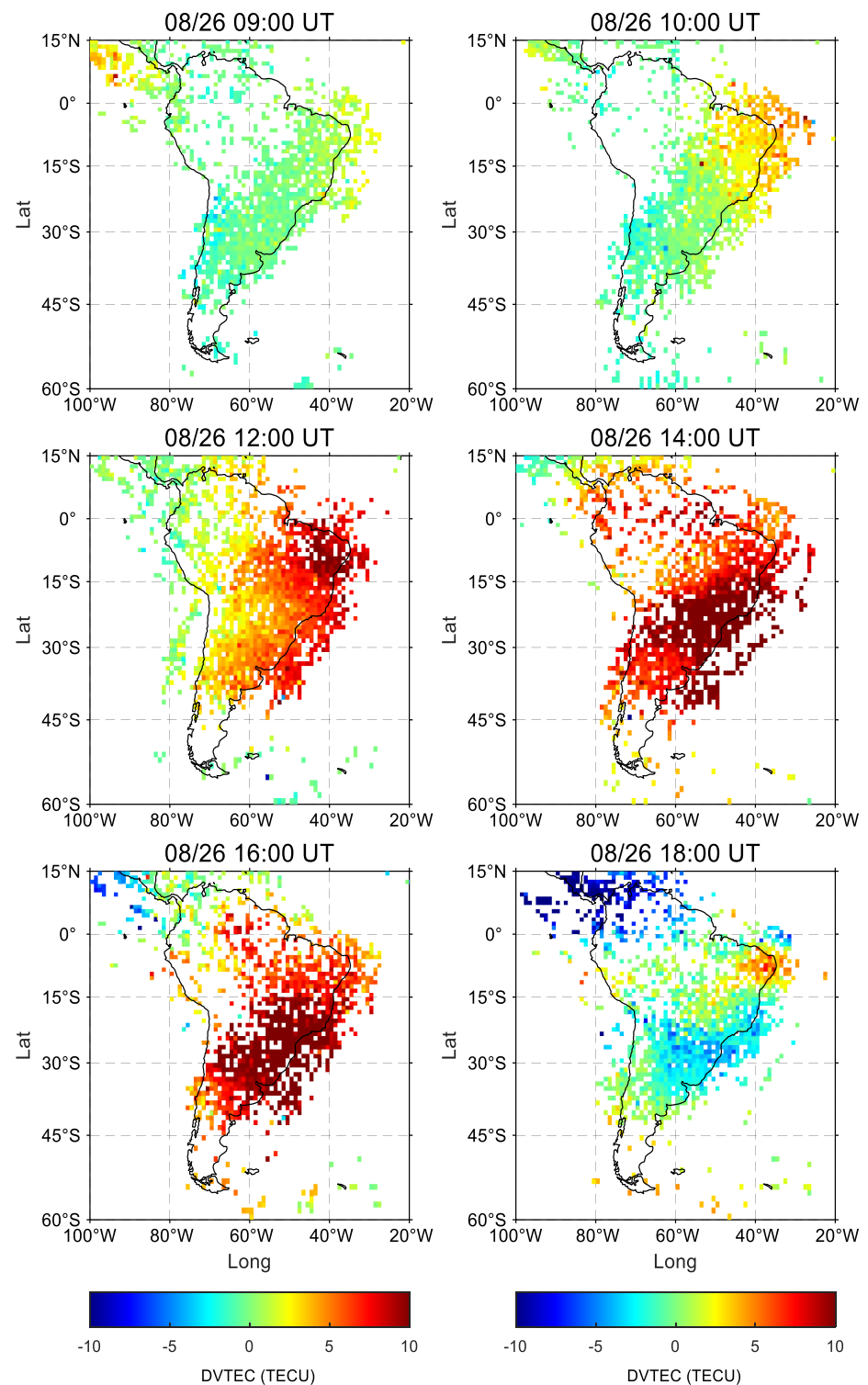


Figure 5. Spatiotemporal evolutions of storm-2.

3.4. Storm-3

Figure 7 shows the distribution of VTEC difference during storm-3. VTEC depletion was first observed in the south and northeast of the North American sector from 00:30 UT on 27 August. At 01:30 UT, the negative storm covered most of the region of North America between 30 and 50° N except the northwest region, and the maximum magnitude was ~10 TECU. From 02:30 UT to 04:30 UT, the VTEC depletion decayed gradually.

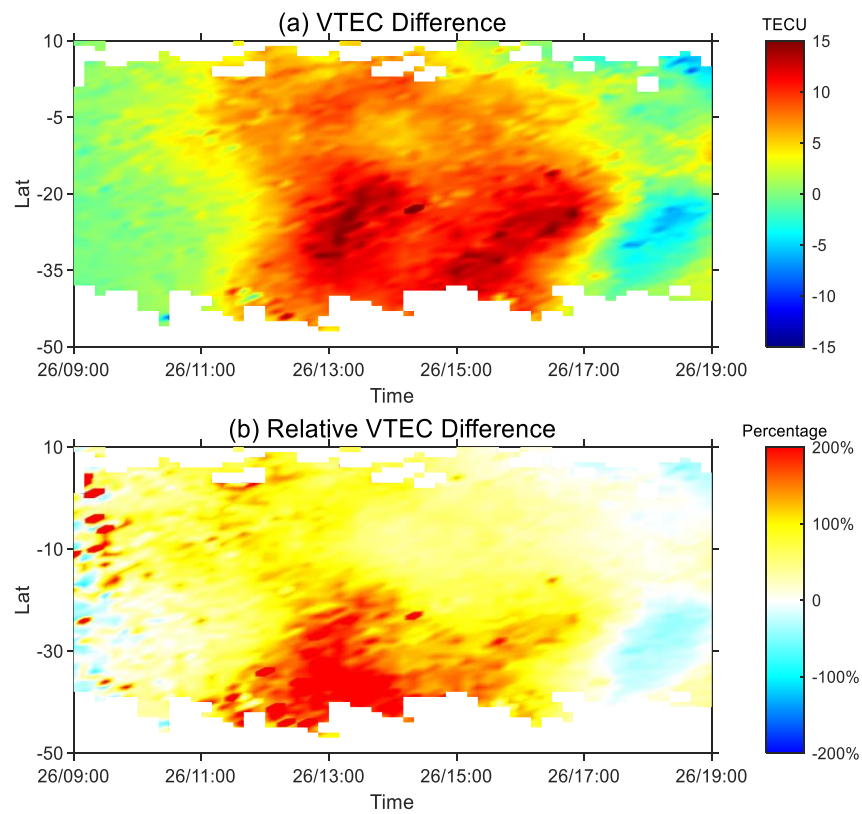


Figure 6. Latitude/time variation of (a) VTEC difference and (b) relative VTEC difference of Storm-2 from 10° N to 50° S at 50° W.

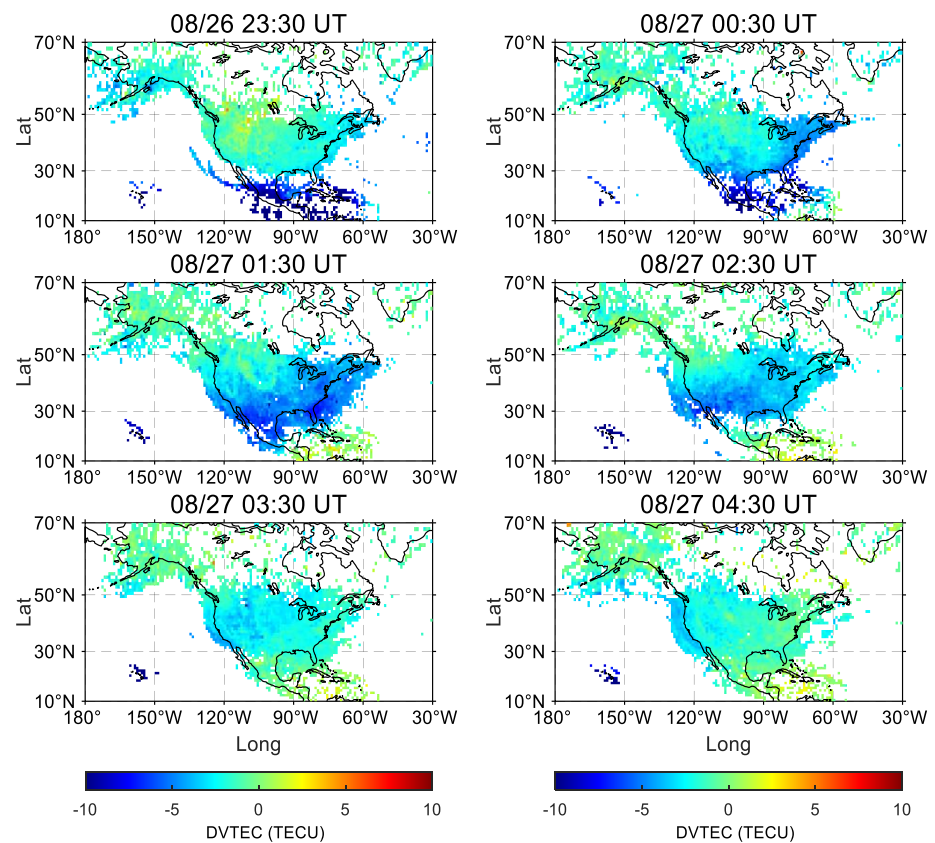


Figure 7. Spatiotemporal evolutions of storm-3.

The latitude/time variation of VTEC difference and relative VTEC difference of storm-3 at 90° W are presented in Figure 8. As we can see in Figure 8a, there was prominent VTEC depletion at low latitudes before the negative storm. The negative disturbance extended from both 30° N and 60° N to 40° N. The time period of the negative storm was from 00:00 UT to 04:30 UT on 27 August and the maximum magnitude was about −10 TECU. In Figure 8b, the relative VTEC difference showed similar magnitude of −60% at low and middle latitudes. Due to the small VTEC background, the relative VTEC difference reached about 100% between 40 and 55° N from 02:00 UT to 05:00 UT, while there was no obvious VTEC reduction after 04:00 UT in absolute VTEC difference.

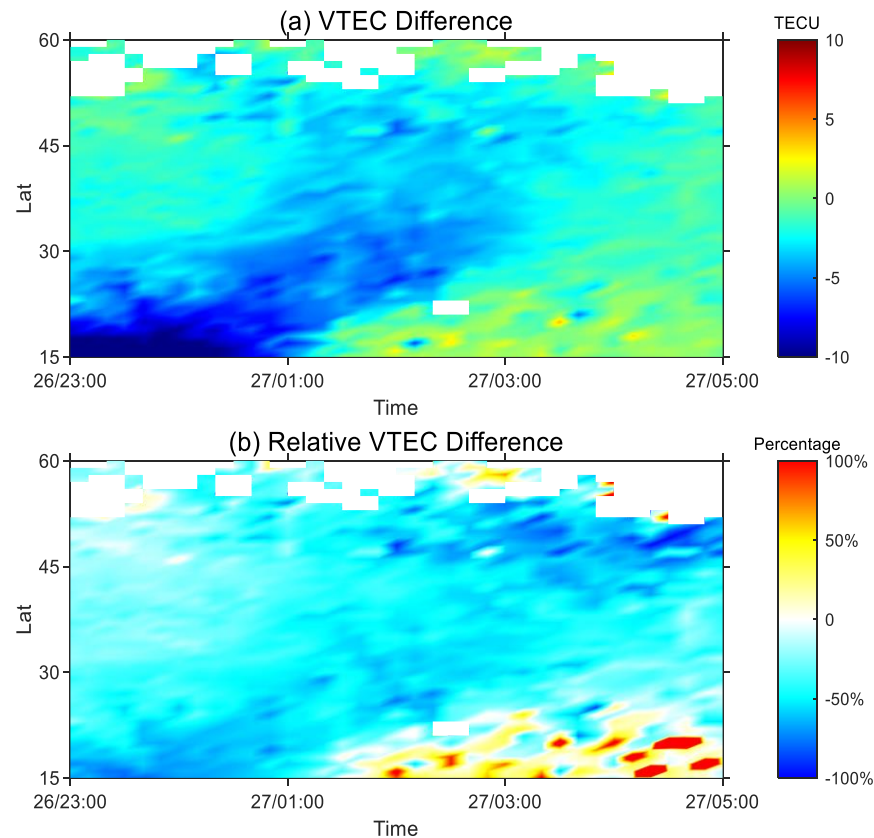


Figure 8. Latitude/time variation of (a) VTEC difference and (b) relative VTEC difference of storm-3 from 15° N to 60° N at 90° W.

3.5. Storm-4

Figure 9 gives the spatiotemporal evolutions of storm 4. This storm exhibited similar evolution to storm 1. At 11:00 UT on 27 August, VTEC enhancement first occurred in the northeast of South America with a magnitude of ~5 TECU. Then, the positive variation expanded from east to west with the magnitude increasing. Between 15:00 and 17:00 UT, the positive storm effect covered most of South America and the maximum magnitude was more than 15 TECU. The VTEC enhancement decayed from 17:00 to 19:00 UT, and only sporadic positive and negative disturbances were observed over the South American sector at 21:00 UT.

Figure 10 shows the latitude/time variation of the VTEC difference and relative VTEC difference of storm-4 at 50° W. As shown in Figure 10a, the positive storm started at ~12:0 UT on 27 August and ended at 19:00 UT. The VTEC enhancement first appeared at low latitudes and extended to higher latitudes. Most of the VTEC increase was about 12 TECU. In Figure 10b, the relative VTEC difference below 25° S was about 90%. During 13:00–16:00 UT, the relative VTEC difference between 40 and 25° S reached ~180%.

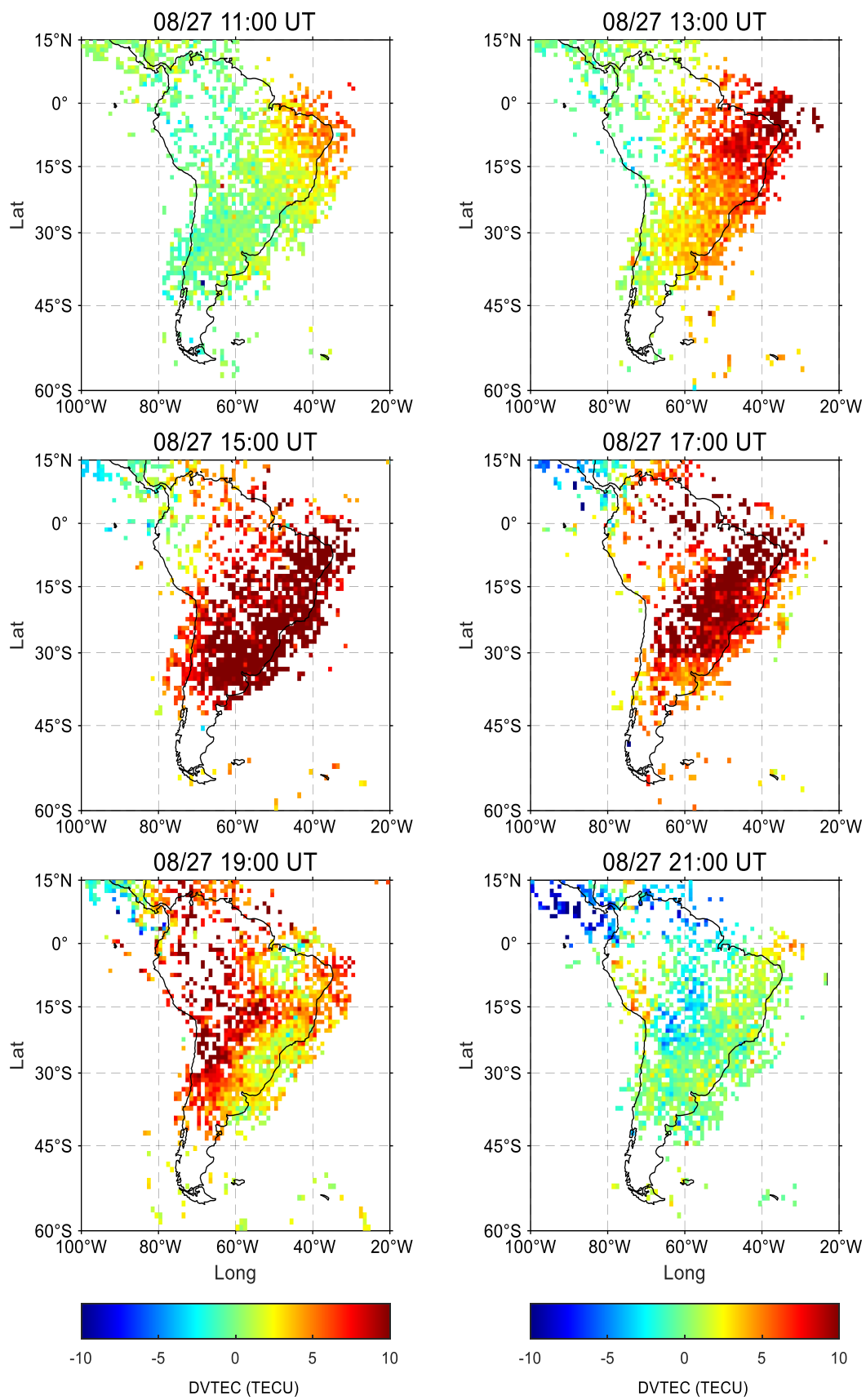


Figure 9. Spatiotemporal evolutions of storm-4.

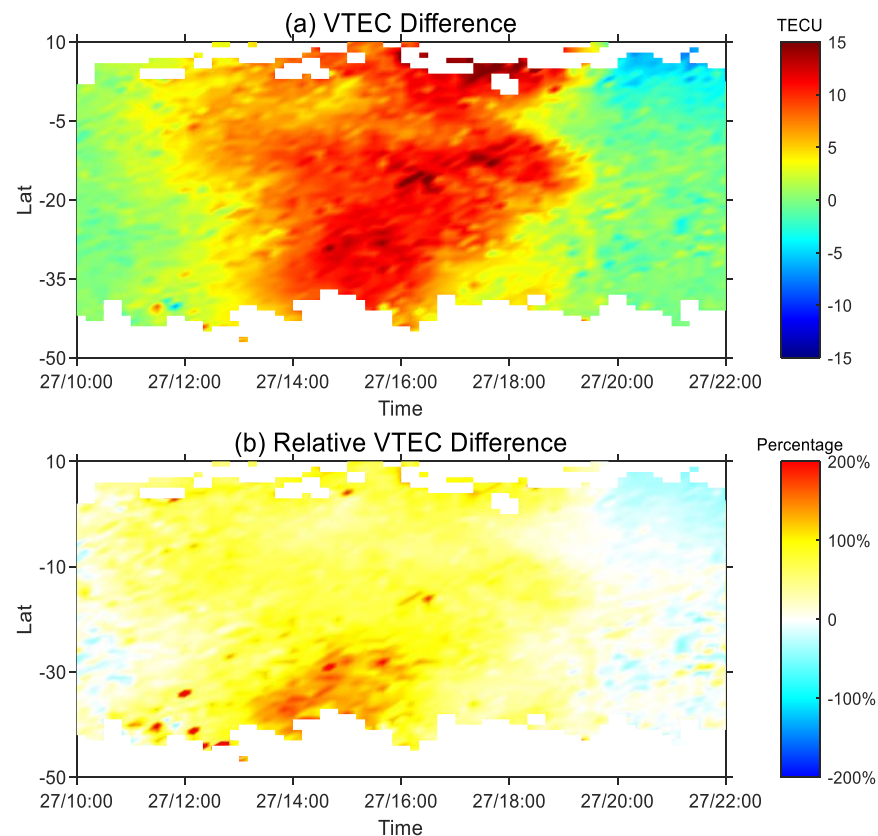


Figure 10. Latitude/time variation of (a) VTEC difference and (b) relative VTEC difference of storm-4 from 10° N to 50° S at 50° W.

3.6. $\Sigma O/N_2$ and Polar Cap Potential Results

Figure 11 shows the $\Sigma O/N_2$ comparisons between the quiet day (left column) and storm days (right column). The rows from the top to the bottom correspond to the North American positive, South American positive 1, North American negative, and South American positive 2 ionospheric storms, respectively. Similar to Figure 11, Figure 12 shows the polar cap potential comparisons between the quiet day (left column) and storm days (right column).

During storm-1, the $\Sigma O/N_2$ ratio was slightly larger than quiet time (Figure 11(a1,a2)). At the same time, the high latitude convection on 25 August expanded and the cross-polar potential was much larger than that on 23 August. The electric field played decisive role in generating storm-1 while the thermospheric composition could also have contributed to that.

As shown in Figure 11(b1,b2), the $\Sigma O/N_2$ ratio for South America (09:00–19:00 UT on 26 August) increased significantly compared with the quiet time. In Figure 12(b1,b2), the polar cap potential map over the magnetic south pole did not expand and the cross-polar potential even decreased. Different from storm-1, storm-2 should be mainly induced by the thermospheric composition variations.

In Figure 11(c1,c2), an $\Sigma O/N_2$ reduction was observed by GUVI, which was related to storm-3. Compared to quiet time, the high latitude electric field over the magnetic north pole expanded at 02:00 UT on 27 August, but the cross-polar cap potential decreased. Further investigation of the relationship between storm-3 and the high latitude electric field is needed.

During storm-4, the $\Sigma O/N_2$ ratio increased from ~ 0.5 (quiet time) to ~ 0.7 over the southern hemisphere. The polar cap potential map over the magnetic south pole expanded but no cross-polar cap potential enhancement occurred. The thermospheric composition variation was responsible for storm-4.

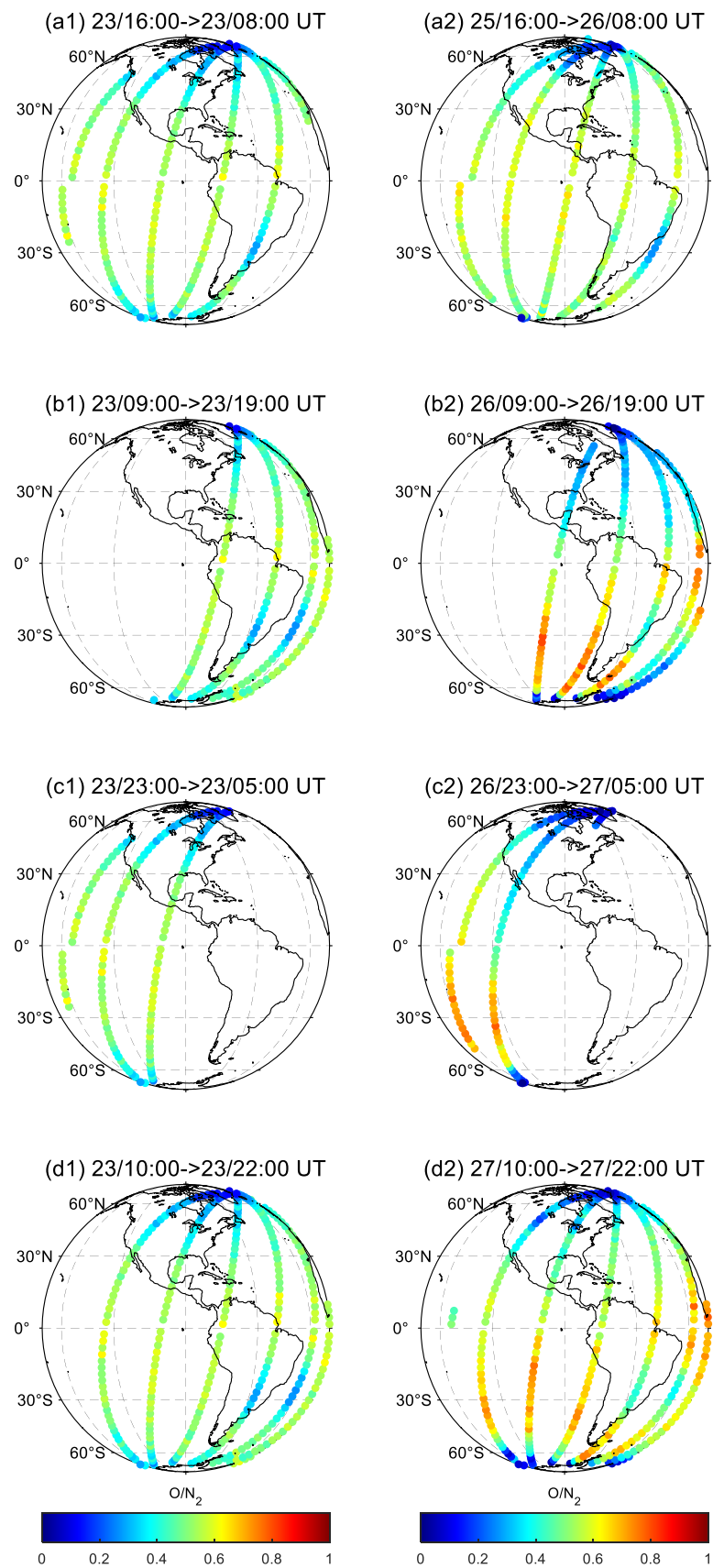


Figure 11. Comparison of $\Sigma O/N_2$ ratio from GUVI between quiet day (left column) and storm days (right column).

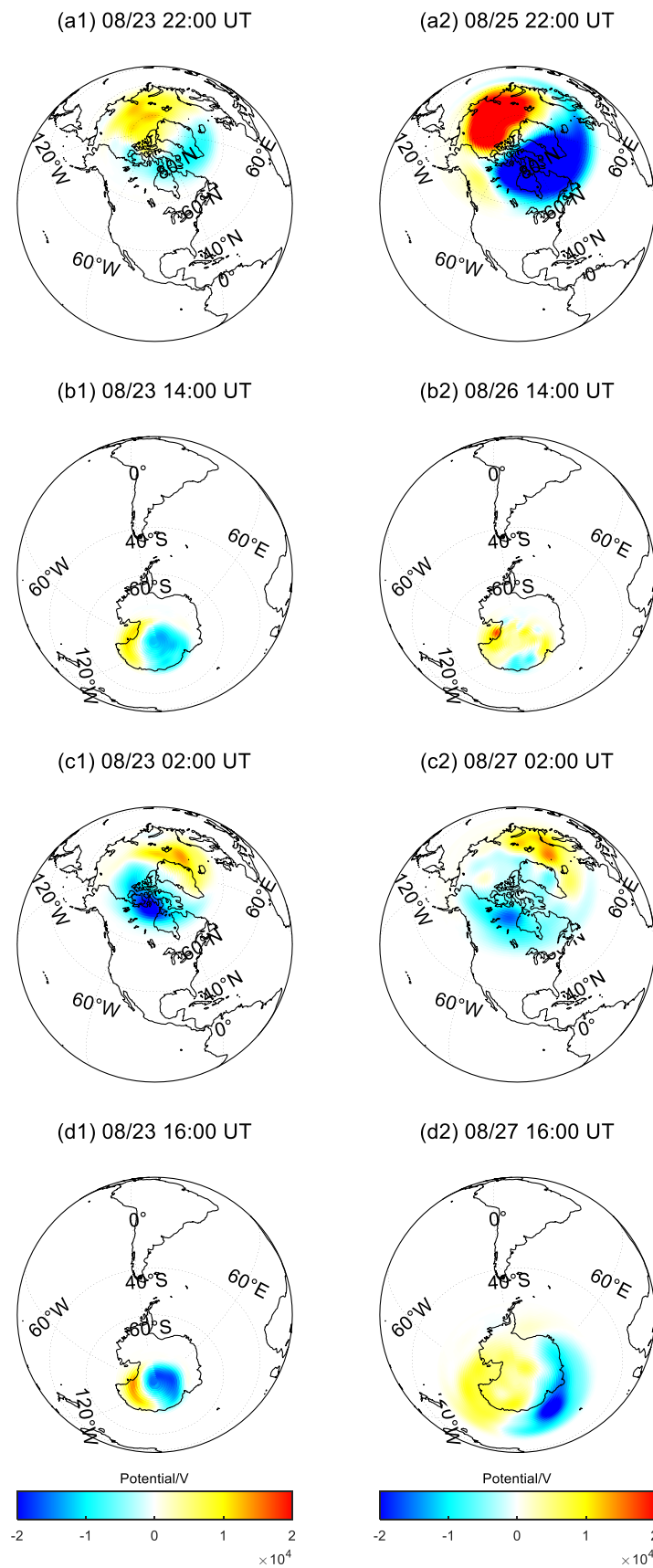


Figure 12. Comparison of polar cap potential map between quiet day (left column) and storm days (right column).

4. Discussion

Akala et al. [29] studied the solar origin of this storm by using multi-instrument observations from the solar surface to the Earth. Their results showed that the storm was induced by a combination of weak CME transients and CIR/HSSs. Electrical currents driven by solar wind penetrated down into the ionosphere and generated PPEFs. During geomagnetic storms, the ionosphere is affected by several factors including electric field, thermosphere composition, and thermospheric neutral wind.

As we can see in Figure 2, prominent hemispheric asymmetries were observed over the American sector during the 25–27 August geomagnetic storm. Astafyeva et al. [30] suggested that seasonal asymmetry in neutral mass density and ionospheric plasma density distributions, along with geomagnetic field asymmetries, played essential roles in the hemispheric asymmetries of ionospheric response. When a positive or negative ionospheric storm appeared in the North American sector, the ionosphere over South America was relatively quiet and vice versa. The background thermospheric neutral wind can influence the ionospheric response to geomagnetic storm significantly. In the summer hemisphere (North America), the quiet time neutral wind is equatorward on the dayside, which is in the same direction with the wind surges. In the winter hemisphere (South America), the background neutral wind opposes the storm induced wind surges. Thus, the neutral wind disturbances in the summer hemisphere are easier to propagate from high latitudes to middle and low latitudes than in the winter hemisphere. In addition, the difference in thermospheric composition and displacement between magnetic and geographic latitude can also contribute to the hemispheric asymmetries during the storm.

Using average value of $\Sigma O/N_2$ for an orbit over each mid- and low-latitudes region, Younas et al. [39] found $\Sigma O/N_2$ enhancement at the northern low latitudes on 26 August, which reached a maximum at 07:00UT with a 23% rise. In Figure 11, compared with the observations on 23 August, there was no significant enhancement over the North American sector. The $\Sigma O/N_2$ increase might occur at other longitudes.

According to Figures 11 and 12, storm-1 was dominated by PPEFs. The VTEC enhancement propagated from high latitudes to middle and low latitudes (Figure 4). However, storm-2 and storm-4, which were induced by thermospheric composition changes, exhibited different propagation direction. The VTEC enhancement expanded from east to west in the longitudinal direction. Although these positive storms were driven by different mechanisms, their magnitudes were similar (~15 TECU).

Storm-3 was generated by O/N_2 decrease over the North American sector, which was similar to the two positive storms occurring in the South American sector (storm-2 and storm-4). However, the VTEC depletion during storm-3 extended from high and low latitudes to mid-latitudes simultaneously, and the absolute maximum magnitude was 10 TECU, which was smaller than storm-2 and storm-4.

5. Conclusions

Three positive ionospheric storms and one negative ionospheric storm were induced by the 25–27 August 2018 geomagnetic storm over the American sector. The GNSS VTEC, GUVI $\Sigma O/N_2$, and SuperDARN polar potential map observations were used to investigate the spatiotemporal variations and mechanisms of these storms.

The VTEC enhancement propagated from high latitudes to middle and low latitudes during the storm-1, and SED and MIT structures were also observed. During the two South American positive storms, the VTEC enhancement both propagated from east to west in the longitudinal direction. The maximum magnitudes of VTEC differences during storm-2 and storm-4 were more than 15 TECU, and the relative VTEC enhancement exceeded 200%. The VTEC depletion during storm-3 extended from both the northeast and south of North America. The maximum magnitude of VTEC difference was about -10 TECU, and the relative VTEC depletion was about -100%.

During storm-1, the high latitude convection expanded and the cross-polar potential was much larger than that on quiet day. The $\Sigma O/N_2$ ratio values also slightly increased.

PPEFs played decisive role in generating storm-1 while the thermospheric composition could also contributed to that.

Comparing with quiet time, the $\Sigma O/N_2$ ratio during the storm-2 increased significantly while the polar cap potential map over the magnetic south pole did not expand and the cross-polar potential even decreased. Different from storm-1, storm-2 should be mainly induced by the thermospheric composition variations.

In storm-3, an $\Sigma O/N_2$ reduction was observed by GUVI. Compared to quiet time, the high latitude electric field over the magnetic north pole expanded at 02:00 UT on 27 August, but the cross-polar cap potential decreased. Thermospheric composition changes should be responsible for storm-3.

During storm-4, the $\Sigma O/N_2$ ratio increased from ~ 0.5 to ~ 0.7 over the southern hemisphere. The polar cap potential map over the magnetic south pole expanded, but no cross-polar cap potential enhancement occurred. The driver of storm-4 was similar to storm-2.

Author Contributions: Conceptualization, X.Y.; Methodology, C.Z. and Y.C.; Validation, C.Z. and X.Y.; Investigation, C.Z.; Data curation, X.C.; Writing—original draft, C.Z.; Writing—review & editing, Y.C. and X.C. All authors have read and agreed to the published version of the manuscript.

Funding: This research was funded by National Natural Science Foundation of China (Grant 42104009), Fundamental Research Funds for the Central Universities (Grant B210201028), China Postdoctoral Science Foundation (Grant 2022M720988).

Data Availability Statement: Publicly available datasets were analyzed in this study. GNSS VTEC data is obtained from Massachusetts Institution of Technology (MIT) (<http://cedar.openmadrigal.org>) (accessed on 21 August 2022). The SuperDARN data are available from <http://vt.superdarn.org> (accessed on 30 August 2022). The GUVI data are obtained from http://guvitimed.jhuapl.edu/data_products (accessed on 25 August 2022).

Conflicts of Interest: The authors declare no conflict of interest.

References

1. Cai, X.; Burns, A.G.; Wang, W.; Qian, L.; Solomon, S.C.; Eastes, R.W.; McClintock, W.E.; Laskar, F.I. Investigation of a Neutral “Tongue” Observed by GOLD During the Geomagnetic Storm on 11 May 2019. *J. Geophys. Res. Space Phys.* **2021**, *126*, e2020JA028817. [[CrossRef](#)]
2. Pedatella, N.M.; Liu, H.L. The Influence of Internal Atmospheric Variability on the Ionosphere Response to a Geomagnetic Storm. *Geophys. Res. Lett.* **2018**, *45*, 4578–4585. [[CrossRef](#)]
3. Aa, E.; Zhang, S.R.; Erickson, P.J.; Coster, A.J.; Goncharenko, L.P.; Varney, R.H.; Eastes, R. Salient Midlatitude Ionosphere-Thermosphere Disturbances Associated with SAPS During a Minor but Geo-Effective Storm at Deep Solar Minimum. *J. Geophys. Res. Space Phys.* **2021**, *126*, e2021JA029509. [[CrossRef](#)]
4. Yu, T.; Wang, W.; Ren, Z.; Cai, X.; Yue, X.; He, M. The Response of Middle Thermosphere (~ 160 km) Composition to the 20 and 21 November 2003 Superstorm. *J. Geophys. Res. Space Phys.* **2021**, *126*, e2021JA029449. [[CrossRef](#)]
5. Yu, T.; Wang, W.; Ren, Z.; Yue, J.; Yue, X.; He, M. Middle-Low Latitude Neutral Composition and Temperature Responses to the 20 and 21 November 2003 Superstorm from GUVI Dayside Limb Measurements. *J. Geophys. Res. Space Phys.* **2021**, *126*, e2020JA028427. [[CrossRef](#)]
6. Zhai, C.; Lu, G.; Yao, Y.; Wang, W.; Zhang, S.; Liu, J.; Peng, W.; Kong, J.; Chen, J. 3-D Tomographic Reconstruction of SED Plume During 17 March 2013 Storm. *J. Geophys. Res. Space Phys.* **2020**, *125*, e2020JA028257. [[CrossRef](#)]
7. Gonzalez, W.; Joselyn, J.-A.; Kamide, Y.; Kroehl, H.W.; Rostoker, G.; Tsurutani, B.; Vasyliunas, V. What is a geomagnetic storm? *J. Geophys. Res. Space Phys.* **1994**, *99*, 5771–5792. [[CrossRef](#)]
8. Yu, T.; Cai, X.; Ren, Z.; Li, S.; Pedatella, N.; He, M. Investigation of the $\Sigma O/N_2$ Depletion with Latitudinally Tilted Equatorward Boundary Observed by GOLD During the Geomagnetic Storm on 20 April 2020. *J. Geophys. Res. Space Phys.* **2022**, e2022JA030889. [[CrossRef](#)]
9. Yu, T.; Wang, W.; Ren, Z.; Cai, X.; Liu, L.; He, M.; Pedatella, N.; Zhai, C. Diagnostic analysis of the physical processes underlying the long-duration $\Sigma O/N_2$ depletion during the recovery phase of the 8 June 2019 geomagnetic storm. *J. Geophys. Res. Space Phys.* **2022**, e2022JA031075. [[CrossRef](#)]
10. Zhai, C.; Tang, S.; Peng, W.; Cheng, X.; Zheng, D. Driver of the Positive Ionospheric Storm over the South American Sector during 4 November 2021 Geomagnetic Storm. *Remote Sens.* **2022**, *15*, 111. [[CrossRef](#)]

11. Zhai, C.; Cai, X.; Wang, W.; Coster, A.; Qian, L.; Solomon, S.C.; Yu, T.; He, M. Mid-Latitude Ionospheric Response to a Weak Geomagnetic Activity Event During Solar Minimum. *J. Geophys. Res. Space Phys.* **2023**, *128*, e2022JA030908. [[CrossRef](#)]
12. Astafyeva, E.; Zakharenkova, I.; Alken, P. Prompt penetration electric fields and the extreme topside ionospheric response to the 22–23 June 2015 geomagnetic storm as seen by the Swarm constellation. *Earth Planets Space* **2016**, *68*, 1–12. [[CrossRef](#)]
13. Buonsanto, M.J. Ionospheric Storms—A Review. *SSRv* **1999**, *88*, 563–601. [[CrossRef](#)]
14. Lu, G.; Goncharenko, L.; Richmond, A.; Roble, R.; Aponte, N. A dayside ionospheric positive storm phase driven by neutral winds. *J. Geophys. Res. Space Phys.* **2008**, *113*. [[CrossRef](#)]
15. Mendillo, M. Ionospheric Total Electron Content Behaviour during Geomagnetic Storms. *NPhS* **1971**, *234*, 23–24. [[CrossRef](#)]
16. Tsurutani, B.; Mannucci, A.; Iijima, B.; Abdu, M.A.; Sobral, J.H.A.; Gonzalez, W.; Guarnieri, F.; Tsuda, T.; Saito, A.; Yumoto, K. Global dayside ionospheric uplift and enhancement associated with interplanetary electric fields. *J. Geophys. Res. Space Phys.* **2004**, *109*. [[CrossRef](#)]
17. Venkatesh, K.; Patra, A.; Balan, N.; Fagundes, P.; Tulasi Ram, S.; Batista, I.; Reinisch, B. Superfountain effect linked with 17 March 2015 geomagnetic storm manifesting distinct F3 layer. *J. Geophys. Res. Space Phys.* **2019**, *124*, 6127–6137. [[CrossRef](#)]
18. Zhao, B.; Wan, W.; Lei, J.; Wei, Y.; Sahai, Y.; Reinisch, B. Positive ionospheric storm effects at Latin America longitude during the superstorm of 20–22 November 2003: Revisit. *Ann. Geophys.* **2012**, *30*, 831–840. [[CrossRef](#)]
19. Balan, N.; Otsuka, Y.; Nishioka, M.; Liu, J.Y.; Bailey, G.J. Physical mechanisms of the ionospheric storms at equatorial and higher latitudes during the recovery phase of geomagnetic storms. *J. Geophys. Res. Space Phys.* **2013**, *118*, 2660–2669. [[CrossRef](#)]
20. Liu, G.; Shen, H. A severe negative response of the ionosphere to the intense geomagnetic storm on 17 March 2015 observed at mid- and low-latitude stations in the China zone. *AdSpR* **2017**, *59*, 2301–2312. [[CrossRef](#)]
21. Sun, W.; Li, G.; Le, H.; Chen, Y.; Hu, L.; Yang, S.; Zhao, X.; Xie, H.; Li, Y.; Zhao, B.; et al. Daytime Ionospheric Large-Scale Plasma Density Depletion Structures Detected at Low Latitudes Under Relatively Quiet Geomagnetic Conditions. *J. Geophys. Res. Space Phys.* **2022**, *127*, e2021JA030033. [[CrossRef](#)]
22. Yue, X.; Wang, W.; Lei, J.; Burns, A.; Zhang, Y.; Wan, W.; Liu, L.; Hu, L.; Zhao, B.; Schreiner, W.S. Long-lasting negative ionospheric storm effects in low and middle latitudes during the recovery phase of the 17 March 2013 geomagnetic storm. *J. Geophys. Res. Space Phys.* **2016**, *121*, 9234–9249. [[CrossRef](#)]
23. Goncharenko, L.; Foster, J.; Coster, A.; Huang, C.; Aponte, N.; Paxton, L. Observations of a positive storm phase on 10 September 2005. *J. Atmos. Sol.-Terr. Phys.* **2007**, *69*, 1253–1272. [[CrossRef](#)]
24. Astafyeva, E.I. Dayside ionospheric uplift during strong geomagnetic storms as detected by the CHAMP, SAC-C, TOPEX and Jason-1 satellites. *AdSpR* **2009**, *43*, 1749–1756. [[CrossRef](#)]
25. Paznukhov, V.; Altadill, D.; Reinisch, B. Experimental evidence for the role of the neutral wind in the development of ionospheric storms in midlatitudes. *J. Geophys. Res. Space Phys.* **2009**, *114*. [[CrossRef](#)]
26. Fuller-Rowell, T.; Codrescu, M.; Moffett, R.; Quegan, S. Response of the thermosphere and ionosphere to geomagnetic storms. *J. Geophys. Res. Space Phys.* **1994**, *99*, 3893–3914. [[CrossRef](#)]
27. Kuai, J.; Liu, L.; Liu, J.; Sripathi, S.; Zhao, B.; Chen, Y.; Le, H.; Hu, L. Effects of disturbed electric fields in the low-latitude and equatorial ionosphere during the 2015 St. Patrick’s Day storm. *J. Geophys. Res. Space Phys.* **2016**, *121*, 9111–9126. [[CrossRef](#)]
28. Danilov, A.D. Ionospheric F-region response to geomagnetic disturbances. *AdSpR* **2013**, *52*, 343–366. [[CrossRef](#)]
29. Akala, A.O.; Oyedokun, O.J.; Amaechi, P.O.; Simi, K.G.; Ogwala, A.; Arowolo, O.A. Solar Origins of 26 August 2018 Geomagnetic Storm: Responses of the Interplanetary Medium and Equatorial/Low-Latitude Ionosphere to the Storm. *SpWea* **2021**, *19*, e2021SW002734. [[CrossRef](#)]
30. Astafyeva, E.; Bagiya, M.S.; Förster, M.; Nishitani, N. Unprecedented Hemispheric Asymmetries During a Surprise Ionospheric Storm: A Game of Drivers. *J. Geophys. Res. Space Phys.* **2020**, *125*, e2019JA027261. [[CrossRef](#)]
31. Bolaji, O.S.; Fashae, J.B.; Adebisi, S.J.; Owolabi, C.; Adebisin, B.O.; Kaka, R.O.; Ibang, J.; Abass, M.; Akinola, O.O.; Adekoya, B.J.; et al. Storm Time Effects on Latitudinal Distribution of Ionospheric TEC in the American and Asian-Australian Sectors: 25–26 August 2018 Geomagnetic Storm. *J. Geophys. Res. Space Phys.* **2021**, *126*, e2020JA029068. [[CrossRef](#)]
32. Blagoveshchensky, D.V.; Sergeeva, M.A. Ionospheric parameters in the European sector during the magnetic storm of 25–26 August 2018. *AdSpR* **2020**, *65*, 11–18. [[CrossRef](#)]
33. Mansilla, G.A.; Zossi, M.M. Ionospheric response to the 26 August 2018 geomagnetic storm along 280° E and 316° E in the South American sector. *AdSpR* **2022**, *69*, 48–58. [[CrossRef](#)]
34. Younas, W.; Amory-Mazaudier, C.; Khan, M.; Fleury, R. Ionospheric and Magnetic Signatures of a Space Weather Event on 25–29 August 2018: CME and HSSWs. *J. Geophys. Res. Space Phys.* **2020**, *125*, e2020JA027981. [[CrossRef](#)]
35. Rideout, W.; Coster, A. Automated GPS processing for global total electron content data. *GPS Solut.* **2006**, *10*, 219–228. [[CrossRef](#)]
36. Vierinen, J.; Coster, A.J.; Rideout, W.C.; Erickson, P.J.; Norberg, J. Statistical framework for estimating GNSS bias. *Atmos. Meas. Tech.* **2016**, *9*, 1303–1312. [[CrossRef](#)]
37. Christensen, A.B. Initial observations with the Global Ultraviolet Imager (GUVI) in the NASA TIMED satellite mission. *J. Geophys. Res.* **2003**, *108*. [[CrossRef](#)]

38. Ruohoniemi, J.; Baker, K. Large-scale imaging of high-latitude convection with Super Dual Auroral Radar Network HF radar observations. *J. Geophys. Res. Space Phys.* **1998**, *103*, 20797–20811. [[CrossRef](#)]
39. Younas, W.; Khan, M.; Amory-Mazaudier, C.; Amaechi, P.O.; Fleury, R. Middle and low latitudes hemispheric asymmetries in $\Sigma O/N_2$ and TEC during intense magnetic storms of solar cycle 24. *AdSpR* **2022**, *69*, 220–235. [[CrossRef](#)]

Disclaimer/Publisher’s Note: The statements, opinions and data contained in all publications are solely those of the individual author(s) and contributor(s) and not of MDPI and/or the editor(s). MDPI and/or the editor(s) disclaim responsibility for any injury to people or property resulting from any ideas, methods, instructions or products referred to in the content.